Full Length Article

A bio-inspired N-doped porous carbon electrocatalyst with hierarchical superstructure for efficient oxygen reduction reaction

Yue-E Miao [a], Jiajie Yan [c], Yue Ouyang [a], Hengyi Lu [c], Feili Lai [c], Yue Wu [b], Tianxi Liu [a,c,*]

[a] State Key Laboratory for Modification of Chemical Fibers and Polymer Materials, College of Materials Science and Engineering, Donghua University, Shanghai 201620, PR China
[b] Research Center for Analysis and Measurement, Donghua University, Shanghai 201620, PR China
[c] State Key Laboratory of Molecular Engineering of Polymers, Department of Macromolecular Science, Fudan University, Shanghai 200433, PR China

ABSTRACT

The bio-inspired hierarchical "grape cluster" superstructure provides an effective integration of one-dimensional carbon nanofibers (CNF) with isolated carbonaceous nanoparticles into three-dimensional (3D) conductive frameworks for efficient electron and mass transfer. Herein, a 3D N-doped porous carbon electrocatalyst consisting of carbon nanofibers with grape-like N-doped hollow carbon particles (CNF@NC) has been prepared through a simple electrospinning strategy combined with in-situ growth and carbonization processes. Such a bio-inspired hierarchically organized conductive network largely facilitates both the mass diffusion and electron transfer during the oxygen reduction reactions (ORR). Therefore, the metal-free CNF@NC catalyst demonstrates superior catalytic activity with an absolute four-electron transfer mechanism, strong methanol tolerance and good long-term stability towards ORR in alkaline media.

1. Introduction

The oxygen reduction reaction (ORR) plays a key role in many important energy-conversion systems, such as metal-air batteries and fuel cells [1–3]. Currently, platinum (Pt) and its alloys dominate the electrocatalyst market for their efficient four-electron transfer ORR process [4,5]. Nevertheless, the large-scale application of Pt is still severely impeded due to the low abundance, high cost, sluggish kinetics and poor stability of noble metals. Upon these technical issues and limitations, intensive research efforts have been devoted to the exploration of efficient and stable nanomaterials with low- or non-Pt usages as high-performance ORR electrocatalysts.

Heteroatom-enriched (*e.g.* nitrogen (N), boron (B), and sulfur (S)) carbon nanomaterials have been considered as promising candidates towards ORR because of their enhanced electrochemical properties, abundant active sites and excellent chemical stabilities [6–8]. The incorporation of heteroatoms within the carbonaceous matrix has been proved to effectively introduce local highly-positive charge density and high spin density to their *ortho*-carbon atoms, thus leading to modulated catalytic sites,

chemisorption energy of O_2 and the consequently enhanced ORR performance [9,10]. Among them, the nitrogen atom with comparable atomic size to carbon and five valence electrons for bonding can bring metallic properties in the carbon nanomaterials through its different N species of pyrrolic N, pyridinic N, graphitic N and amino N [11,12]. As a result, a variety of N-doped carbonaceous materials with hierarchical structures, such as porous N-doped graphene frameworks [13,14], integrated carbon nanofiber@N-doped graphene blends [15,16], N-doped carbon materials [17], and N-doped carbon nanosheets assembly from polyimide [18,19], have been reported to show remarkably strengthened initial chemical adsorption of oxygen and largely increased possible active sites for oxygen reduction reactions. At the same time, however, the easily changed conduction/valence band position of the heteroatom-doped carbon materials results in the opened bandgap and intrinsic barrier that hinder further charge transfer [20,21]. Therefore, it still remains a great challenge to properly balance the competition between the density of active sites and conductivity when developing heteroatom-doped carbonaceous catalysts.

Along with the heteroatom doping strategy, the creation of porous architectures in the carbon nanomaterials with different pore sizes can afford large surface area for fast mass transport and highly exposed active sites for efficient catalytic reactions [22–24]. Taking this into account, a family of mesoporous nonprecious metal catalysts with outstanding half-wave ($E_{1/2}$) potential of 0.79 V (only ∼58 mV deviation from Pt/C), high selectivity (electron-

transfer number > 3.95), and excellent electrochemical stability has been prepared by using the ordered mesoporous silica and layered montmorillonite clay with two-dimensional open channels as the hard templates [25]. Nevertheless, the lack of connection between these isolated nanoparticles inevitably gives rise to the low conductivities of the catalysts. Hence, much more efforts should be devoted to improving the conductivity of the porous carbon nanoparticles by linking them with various conductive backbones.

In nature, the bunch of grapes efficiently delivers nutrition into each grape through its main stem. Inspired by this unique feature of the tight and continuous contact between each grape particle with the central plant stem, we have designed a porous N-doped carbon electrocatalyst with a novel hierarchical "grape cluster" superstructure. The porous N-doped carbon electrocatalyst consists of one-dimensional (1D) carbon nanofibers integrated with grape-like N-doped hollow carbon particles as illustrated in Fig. 1a, forming a favorable three-dimensional (3D) conductive network. Thus, the mass diffusion/oxygen molecule adsorption can be efficiently facilitated on the surface of the active sites of the N-doped carbon particles. Meanwhile, the inner conductive carbon nanofiber backbone guarantees fast electron transfer to the catalytic active sites for efficient oxygen reduction reactions.

To obtain the hierarchical "grape cluster" superstructure, grape-like FeOOH particle decorated polyacrylonitrile (PAN) nanofibers (PAN@FeOOH) were obtained first through the hydrothermal reaction of ferric chloride hexahydrate in the presence of the PAN nanofiber template as illustrated in Fig. 1b. Subsequently, in-situ polymerization of dopamine was carried out to prepare polydopamine (PDA) coated PAN@FeOOH (PAN@FeOOH@PDA) composite fibers. Then, the PAN@FeOOH@PDA composite was thermally treated under an inert atmosphere to obtain 1D carbon nanofibers decorated with yolk-shell Fe_3O_4@PDA-derived carbon particles, that is, the CNF@Fe_3O_4@NC composite. After etching with acid, Fe_3O_4 in the CNF@Fe_3O_4@NC composite was removed to obtain the final CNF@NC composite with the hierarchical "grape cluster" superstructure, which consists of carbon nanofibers integrated with grape-like N-doped hollow carbon particles. The efficient overlap and merging of the conductive carbon nanofiber framework with the grape-like hollow NC particles through the thin layer of polydopamine-derived carbon can ultimately lead to a three-dimensionally interconnected N-doped carbonaceous electrocatalyst, which exhibits superior activity and stability compared to those of the commercial Pt/C electrode towards ORR in alkaline media.

2. Experimental section

2.1. Reagents

PAN (Mw $\approx$ 150 000) was purchased from Sigma–Aldrich. Ferric chloride hexahydrate ($FeCl_3 \cdot 6H_2O$), nitric acid (69%), hydrochloric acid (36.5%), ethylene glycol (EG) and $H_2PtCl_6 \cdot 6H_2O$ were supplied by Sinopharm Chemical Reagent Co., Ltd. Dopamine hydrochloride (98%) was obtained from Aladdin Chemical Reagent. Tris(hydroxy methyl)aminomethane (TRIS, 99%) and tris(hydroxylmethyl)amino methane hydrochloride (TRIS·HCl, 99%) were purchased from Alfa Aesar. Deionized water was used as solvent for all experiments. All other reagents were of analytical grade and used without further purification.

2.2. Preparation of electrospun PAN nanofibers

Firstly, PAN was dissolved in *N,N*-dimethylformamide (DMF) under vigorous stirring at room temperature for 12 h to prepare a 10 wt% homogeneous solution for electrospinning. Then, the solution was loaded into a syringe equipped with a stainless steel needle. During the electrospinning process, a voltage of 12 kV and a feeding rate of 1 mL h^{-1} were applied to the spinneret. After 60 min of electrospinning, a non-woven PAN membrane was generated and could be easily peeled off from the aluminum drum collector. Then the obtained membrane was pre-oxidized under an air atmosphere at 250 °C for 1 h with a heating rate of 1 °C min^{-1} for further use.

2.3. Synthesis of hierarchical PAN@FeOOH and PAN@FeOOH@PDA

For a typical run, 0.1 g of as-prepared pre-oxidized PAN membranes were immersed into $FeCl_3 \cdot 6H_2O$ solution (0.05 M) at 90 °C for 12 h. After that, the membranes were rinsed for three times with deionized water to remove the residual $FeCl_3$ solution. Subsequently, PDA-coated PAN@FeOOH fibers were prepared according to our previous report. Briefly, the PAN@FeOOH fibers were immersed in a freshly prepared aqueous solution of dopamine (1 mg mL^{-1} in 10 mM Tris buffer, pH = 8.5) at room temperature for 5 h. After the reaction, the fibers were washing with a large amount of deionized water, and then overnight dried at 60 °C in a vacuum oven. For comparison, PDA-coated FeOOH (FeOOH@PDA) nanoparticles without the PAN template were also prepared under the same procedures.

2.4. Synthesis of CNF@Fe_3O_4@NC, CNF@NC and CNF@NC@Pt

The as-obtained PAN@FeOOH@PDA membranes were transferred into a crucible and annealed in N_2 at 800 °C with a ramp rate of 5 °C min^{-1} for 2 h to yield the carbon nanofibers decorated with yolk-shell Fe_3O_4@PDA-derived carbon particles (CNF@Fe_3O_4@NC). Finally, the CNF@Fe_3O_4@NC was treated with a rotation of HCl and HNO$_3$ solution at room temperature for 144 h and then obtained the aimed carbon material with "grape cluster" hierarchical structure (CNF@NC). Furthermore, CNF@NC-T (with increased wall thickness of the NC particles) and CNF@NC-B (with larger size of the NC particles) hierarchical nanofibers were also prepared under the same immersion solution with different concentrations, that is 2 mg mL^{-1} dopamine for CNF@NC-T and 0.1 M $FeCl_3 \cdot 6H_2O$ solution for CNF@NC-B. Similarly, the contrast sample of FeOOH@PDA was turned into Fe_3O_4@NC and NC particles respectively.
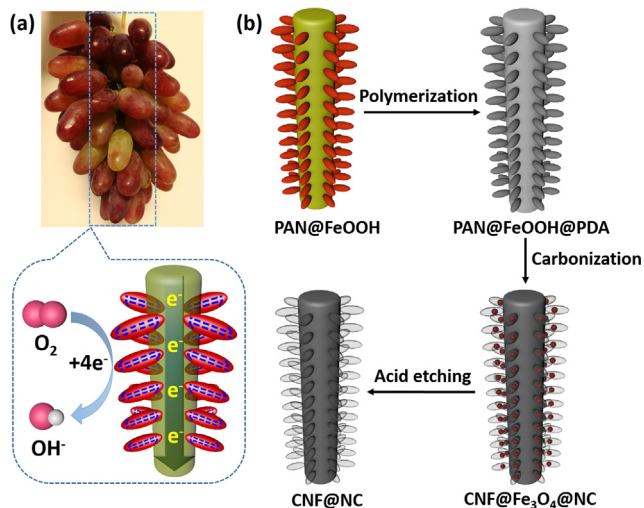

Fig. 1. (a) The schematic construction of bio-inspired conductive paths. (b) Schematic illustration for the preparation of the CNF@NC composite.

To prepare Pt-loaded CNF@NC (CNF@NC@Pt) composite, the CNF@NC was dispersed in a mixture of EG and water by ultrasonication. Then, the $H_2PtCl_6 \cdot 6H_2O$ precursor was dropwise added to the suspension in 1 h at specific concentrations (i.e., 5, 10, 20 and 30 mg mL^{-1}) and further stirred for 1 h. After that, the reaction solution was maintained at 140 °C for 4 h in N_2 atmosphere under magnetic stirring and reflux conditions to ensure that all the Pt nanoparticles were completely reduced. Finally, the slurry was centrifuged and washed with distilled water and acetone to obtain the final product. After thoroughly dried in the vacuum oven, the Pt-loaded composites were labeled as CNF@NC@Pt-5, CNF@NC@Pt-10, CNF@NC@Pt-20 and CNF@NC@Pt-30 respectively for further use.

2.5. Characterization

Morphology of the samples was observed using a field emission scanning electron microscope (FESEM, Zeiss) at an acceleration voltage of 5 kV. Transmission electron microscopy (TEM) was performed under an acceleration voltage of 200 kV with a Tecnai G2 20 TWIN TEM. Specific surface area and pore size distribution of the samples were measured by nitrogen adsorption-desorption method at 77 K (Micromeritics Tristar ASAP 3000) using Brunauer-Emmett-Teller (BET) method. X-ray diffraction (XRD) experiments were conducted from $2\theta = 10°$ to $80°$ on an X'Pert Pro X-ray diffractometer with Cu K$_\alpha$ radiation ($\lambda = 0.1542$ nm) under a voltage of 40 kV and a current of 40 mA. X-ray photoelectron spectroscopy (XPS) analyses were performed with a Thermo Scientific ESCALAB 250Xi using an Al K$_\alpha$ source 1846.6 eV anode. All XPS spectra were corrected using a C 1s line at 285 eV. Curve fitting and background subtraction were accomplished using XPS PEAK41 software.

2.6. Eelectrochemical measurements

The ORR activity of all samples was tested in a conventional three-electrode cell using a CHI 600 electrochemical workstation (Shanghai Chenhua Instrument Co., China) equipped with a rotating electrode setup. The Ag/AgCl electrode and carbon rod were used as the reference electrode and counter-electrode, respectively. The rotating ring-disk electrode (RDE) loaded with various catalysts were used as the working electrodes. The CNF@NC catalysts were prepared by cutting the membranes into slices with a diameter of ca. 0.5 cm, which were directly deposited on the RDE with 5 μL of Nafion solution (5 wt%, Sigma–Aldrich) as electric binder. For comparison, the control catalyst of the commercial Pt/C was prepared by dispersing 2 mg of the samples in 200 μL of water along with 20 μL Nafion (5 wt% in ethanol) and sonicated for at least 15 min to form a homogeneous emulsion. Finally, 3.5 μL of the above slurry was dropped onto the RDE to form Pt/C modified RDE. All electrochemical tests were conducted at room temperature in 0.1 M N_2 or O_2-saturated KOH aqueous solution.

The electron transfer number (n) and kinetic current density (J_k) were investigated based on the Koutecky-Levich (K-L) equation:

$$\frac{1}{J} = \frac{1}{J_L} + \frac{1}{J_k} = \frac{1}{B\omega^{1/2}} + \frac{1}{J_k} \tag{1}$$

$$B = 0.2nFC_o(D_o)^{2/3}\nu^{-1/6} \tag{2}$$

where J is the measured current density, J_k is the kinetic current density, J_L is the diffusion current density, ω is the electrode rotation rate, F is the Faraday constant (96 485 C mol^{-1}), C_o is the bulk concentration of O_2 (1.2×10^{-6} mol cm^{-3}), D_o is the diffusion coefficient of O_2 (1.9×10^{-5} cm^2 s^{-1}), and ν is the kinetic viscosity of the electrolyte (0.01 cm^2 s^{-1}). Here, the constant 0.2 is adopted when the rotating rate is expressed in rpm.

3. Results and discussion

As displayed in the SEM images of Fig. 2a, electrospun PAN nanofibers exhibit uniform diameter with an average size around 280 nm. In order to mimic the hierarchical superstructure of "grape cluster", grape-like FeOOH particles with length of ∼170 nm and diameter of ∼60 nm (Fig. 2b) are uniformly grown on the surface of PAN nanofibers to obtain PAN@FeOOH composite. PDA, behaving as both the precursory N-doping agent and conductive linker, is then coated on the surface of the PAN@FeOOH composite fibers to achieve PAN@FeOOH@PDA composite [26–28]. As exhibited in Fig. 2c, larger particle size is observed for the PDA coated FeOOH (FeOOH@PDA) particles in the PAN@FeOOH@PDA composite compared to that of the FeOOH particles in the PAN@FeOOH composite, indicating that PDA exists as a thin and uniform coating layer on the surface of the PAN@FeOOH composite fibers. Subsequently, the FeOOH@PDA particles are turned into Fe_3O_4@-PDA-derived carbon particles (Fe_3O_4@NC) with grape-like yolk-shell structures after carbonization, while the inside PAN nanofiber frameworks form 1D carbon nanofibers (Fig. 2d). As further illustrated in Fig. S1a, Fe_3O_4 nanoparticles show diameter around 80 nm while a thin layer of N-doped carbon is formed outside the CNF@Fe_3O_4 composite, which fully replicates the hierarchical architecture of the "grape cluster". Thus, the PDA-derived N-doped carbon layer effectively acts as the tight and conductive linking and bonding agent between the Fe_3O_4 nanoparticles and CNF template in the CNF@Fe_3O_4@NC composite. Besides, mesopores are facilely constructed in the non-precious N-doped carbonaceous CNF@NC networks after the removal of Fe_3O_4 nanoparticles (Fig. 2e). We also purposely find a cross-section SEM image of one stripped CNF@NC composite fiber as shown in Fig. 2f. As expected, the grape-like NC particles are evenly and tightly integrated on the surface of the PAN-derived CNF nanofiber by the thin layer of PDA-derived carbon, thus to form the hierarchical superstructure which will be beneficial to fast mass diffusion and higher catalytic reaction rate on the more exposed active sites compared to the smooth surface of CNFs. For comparison, the grape-like NC particles were also prepared under similar reaction conditions but without the PAN nanofiber template. As shown in Fig. S1b, during the intermediate step of the synthetic process, the grape-like yolk-shell structure is also observed for the Fe_3O_4@-NC particles, which further forms severely aggregated grape-like NC particles after the acid etching of Fe_3O_4 (Fig. S2).

The structure of the samples was investigated by XRD. As shown in Fig. 2 g, PAN is almost completely amorphous and exhibits a weak broad halo at $2\theta = 16.9°$. Meanwhile, sharp peaks at $2\theta = 12.1°$, $17.0°$, $27.0°$ and $35.7°$ are observed for PAN@FeOOH and PAN@FeOOH@PDA composites, which are indexed to the (110), (200), (310) and (211) planes of the β-FeOOH (JCPDS 34-1266) with good crystallinity [29,30]. After carbonization, characteristic peaks occur at $2\theta = 30.3°$, $35.7°$, $43.2°$, $57.1°$ and $62.9°$ corresponding to the (220), (311), (400), (511) and (440) diffraction planes of the Fe_3O_4 crystal (JCPDS 19-0629) in the CNF@Fe_3O_4@NC composite [31], which demonstrates the successful transition from β-FeOOH to Fe_3O_4 after high-temperature thermal treatment. The chemical composition of CNF@Fe_3O_4@NC was further analyzed by XPS measurement. As exhibited in Fig. S3, the Fe 2p signal is observed along with C 1s, O 1s, and N 1s signals. Moreover, the inset high-resolution spectrum of Fe 2p shows two typical peaks at the binding energies of 710.3 eV and 724.2 eV, which are assigned to Fe 2p$_{3/2}$ and Fe 2p$_{1/2}$ [32], respectively. The survey scan spectrum of CNF@NC also shows obvious C1s, O1s, and N1s signals
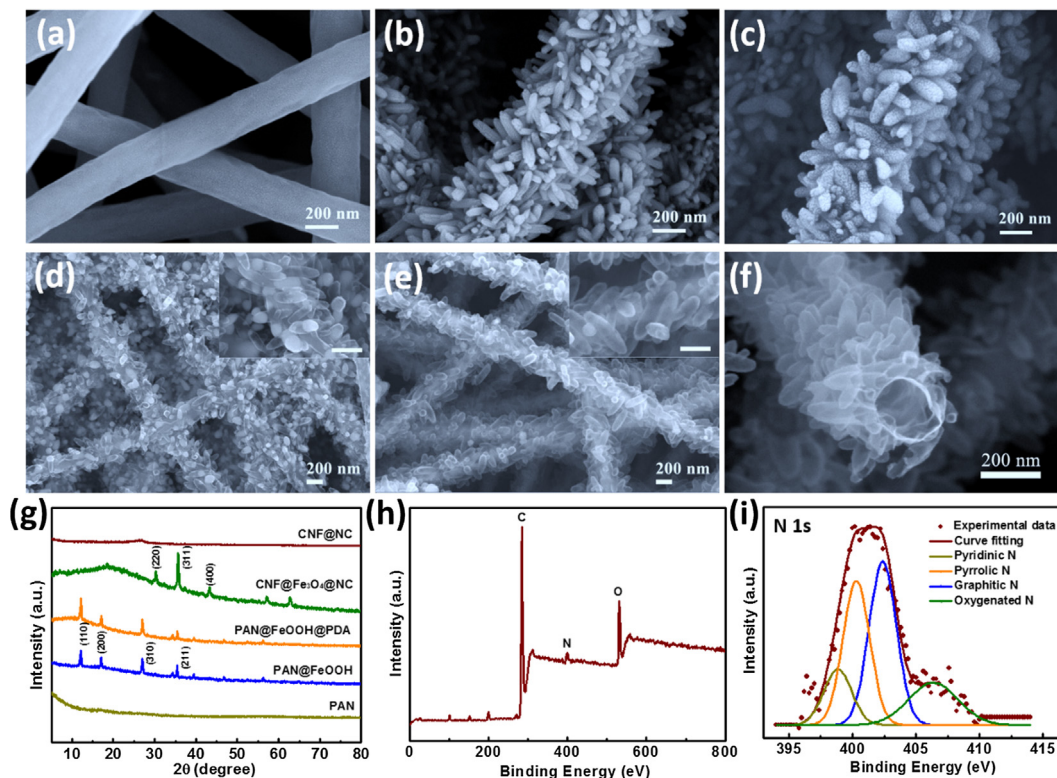
Fig. 2. SEM images of different samples: (a) PAN nanofibers, (b) PAN@FeOOH, (c) PAN@FeOOH@PDA, (d) CNF@Fe$_3$O$_4$@NC, and (e) CNF@NC composites (the insets of d and e show the corresponding higher magnification images). (f) The corresponding cross-section SEM image of the CNF@NC composites. (g) XRD patterns of the samples. (h) The survey scan XPS spectrum of the CNF@NC composite. (i) The corresponding high-resolution XPS spectrum of N 1s in the CNF@NC composite.

(Fig. 2h), confirming the successful doping of nitrogen into the CNF@NC nanofibers and efficient removal of Fe$_3$O$_4$. Particularly, the atomic content of nitrogen is found to be higher than 8% in the hierarchical CNF@NC composite. To further analyze the chemical state of nitrogen, the high-resolution spectrum of N1s is fitted into four signals located at binding energies of 398.8 eV, 400.3 eV, 402.3 eV and 406.3 eV (Fig. 2i), which are originated from the pyridinic-N, pyrrolic-N, graphitic-N and oxygenated N [33,34], respectively. It is worth noting that the graphitic-N keeps a dominant percentage in the CNF@NC electrocatalyst, indicating a higher doping efficiency of the N heteroatom in the sp^2 carbon network structure.

To further explore the inside porous structure of CNF@NC, BET nitrogen adsorption-desorption isotherms were measured. As shown in Fig. 3a, much higher BET surface area (338 m^2 g^{-1}) is achieved for CNF@NC compared to that (94 m^2 g^{-1}) of pure CNFs. The corresponding Barrett-Joyner-Halenda pore-size-distribution curve of the CNF@NC composite (Fig. 3b) shows a narrow peak located around 3–4 nm and a broad peak around 40 nm, indicating the successful construction of hierarchical mesopores in the CNF@NC composite. Thus, higher porosity and larger specific surface area will be afforded for both sufficient contact between the adsorbed oxygen molecules and the electrocatalyst and the rapid electron transfer along the hierarchically organized mesoporous conductive frameworks. Additionally, the size-defined mesopores are facilely tuned by adjusting the size of the hard template of Fe$_3$O$_4$ and the thickness of the PDA coating layer. Through increasing the initial concentration of the dopamine precursor, increased wall thickness of the PDA-derived carbon coating layer is achieved for the CNF@Fe$_3$O$_4$@NC composite (signed as CNF@Fe$_3$O$_4$@NC-T,
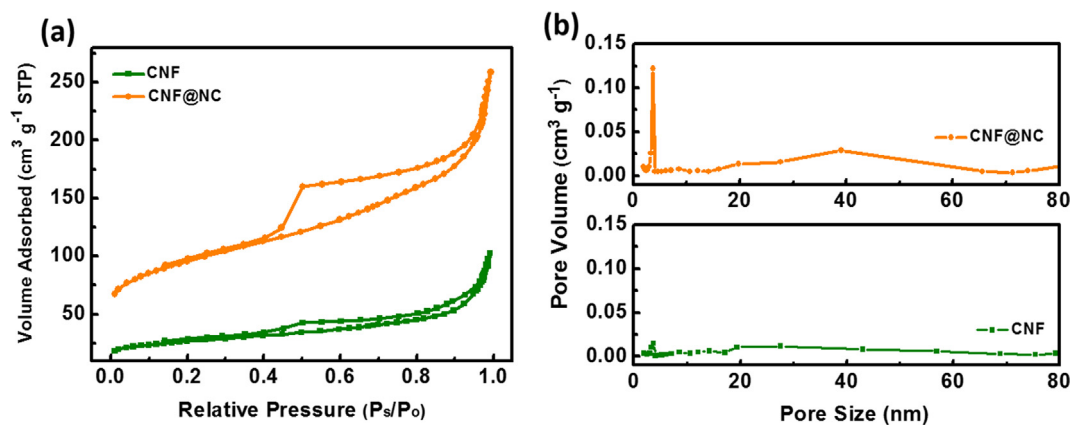

Fig. 3. (a) Nitrogen adsorption-desorption isotherms and (b) the corresponding pore size distribution plots of pure CNF and CNF@NC composite.

Fig. 4a and b). After etching with acid, the corresponding CNF@NC-T composite was obtained (Fig. 4c). However, the NC-T particles seem to be very densely packed with each other on the surface of the CNF matrix, which may affect the following mass/electron transfer processes. For comparison, the CNF@Fe_3O_4@NC composite derived from PAN@FeOOH@PDA composite anchored with larger Fe_3O_4 particles is also obtained in Fig. 4d and 4e, which is signed as CNF@Fe_3O_4@NC-B. Thus, the CNF@NC-B composite (Fig. 4f) was prepared after the complete removal of Fe_3O_4 particles. Obviously, the grape-like NC-B particles show much larger length (300 nm) and diameter (120 nm) than those of the NC particles as displayed in Fig. 2f, which results in a much lower loading density of the NC-B particles than that in the CNF@NC composite.

To evaluate the electrocatalytic ORR activity of the samples, CV measurements were carried out in O_2-saturated 0.1 M KOH aqueous solution at a scan rate of 5 mV s^{-1} (Fig. 5a). Characteristic cathodic peaks are clearly detected for all the samples in O_2-saturated electrolytes, implying their electrocatalytic activities. Furthermore, all of the CNF@NC composites exhibit more positive cathodic peak (E_{peak}) potentials (0.74 V, 0.75 V, and 0.67 V for CNF@NC, CNF@NC-T and CNF@NC-B, respectively) than those of pure CNF (0.63 V) and NC (0.62 V). The poor current response of NC towards ORR should be ascribed to the relatively severe aggregation and poor conductivity of the isolated NC particles. In contrast, the CNF electrode exhibits higher current response compared to that of NC, which can be derived from the intertwined 3D conductive network structure. Therefore, when the NC particles are effectively linked by the CNF template to form the hierarchical "grape cluster" superstructures, the bio-inspired conductive paths are efficiently constructed for fast electron transfer from the main stem to each single NC particle. Thus, the catalytic reactions of the adsorbed O_2 are powerfully promoted on the active sites of the surface of each NC particle as illustrated in Fig. 1a.

To further assess the electrocatalytic activities of the CNF@NC composites, LSV curves were investigated using the rotating ring-disk electrode in O_2-saturated 0.1 M KOH at a rotation speed of 1600 rpm. As depicted in Fig. 5b, all of the CNF@NC composites present more positive onset potentials and larger current densities compared to pure CNF and NC. This could be ascribed to the efficient 3D conductive pathways provided by the CNF backbone, as well as the nitrogen-induced charge delocalization and high hydrophilicity of the highly porous NC particles for efficient oxygen adsorption [9,15]. It can be observed that the CNF@NC composite with a proper pore size shows a very high limited current density of 7.7 mA cm^{-2} at 0.589 V vs. reversible hydrogen electrode (RHE), which is much higher than those of CNF (3.2 mA cm^{-2}), NC (2.0 mA cm^{-2}), CNF@NC-T (5.5 mA cm^{-2}), and CNF@NC-B (6.4 mA cm^{-2}). Especially, only with a proper size of the hollow NC particle, the CNF@NC composite can guarantee both a high limited current density and good stability.

LSV measurements at various rotation speeds also have been collected to reveal the reaction kinetics of O_2 on the surface of CNF@NC, pure CNF and NC electrocatalysts as displayed in Fig. S4a–c. It can be observed that the current densities of the different electrocatalyst modified RDEs increase with increasing the rotation rate from 400 to 2025 rpm, suggesting the increased diffusion rate at high rotation speeds. Then, the corresponding Koutecky-Levich (K-L) plots (J^{-1} vs. $\omega^{-1/2}$) of CNF@NC, pure CNF and NC electrocatalysts are obtained at various potentials to thoroughly investigate their kinetic electron reaction mechanisms. As shown in Fig. S4d–f, the K-L plots almost parallel with each other to show good linearity for each sample, suggesting the first-order reaction kinetics in proportion to the concentration of dissolved oxygen. Consequently, the electron transfer number (n) of the CNF@NC composite is calculated to be 4.0 over the potential range from 0.3 to 0.6 V (Fig. 5c), which reveals a preferred 4e$^-$ oxygen reduction process. In contrast, the pure CNF and NC exhibit lower n values of 3.5 and 2.4, indicating a combined pathway of 2e$^-$ and 4e$^-$ reductions and a dominated two electron-transfer involving peroxide as the intermediate, respectively. According to previous reports [35,36], the poor electron transfer to the adsorbed O_2 molecules often occurs in some metal-free electrocatalysts, which may result in a low selectivity for the four-electron reduction. Despite all this, the above results indicate that the rationally designed N-doped carbonaceous electrocatalyst with bio-inspired "grape cluster" superstructure in this work is efficient to be considered as a high-performance metal-free carbonaceous electrocatalyst towards ORR.

To ensure a high energy conversion efficiency of the fuel cells and air batteries, the working potential of the cathode should be maintained as high as that of the commercial Pt/C catalyst. Therefore, the RDE measurements were further conducted on CNF@NC and the commercial Pt/C under the same conditions (Fig. 5d). Remarkably, by taking the $E_{1/2}$ potential as a comparative standard during ORR, the CNF@NC composite exhibits a relatively positive $E_{1/2}$ value (0.72 V) with only a very small difference (0.12 V) to that (0.84 V) of Pt/C. Besides, the CNF@NC catalyst manifests a much higher kinetic current density (7.7 mA cm^{-2}) compared to that (4.4 mA cm^{-2}) of the Pt/C electrode. As displayed in Table S1, the $E_{1/2}$ potential and limited diffusion current density of the materials
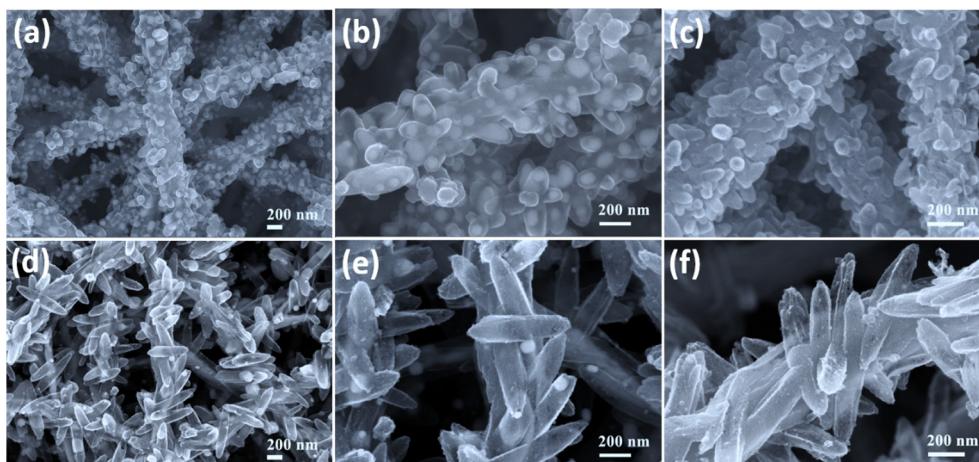

Fig. 4. SEM images of (a, b) CNF@Fe_3O_4@NC-T, (c) CNF@NC-T, (d, e) CNF@Fe_3O_4@NC-B and (f) CNF@NC-B composites.
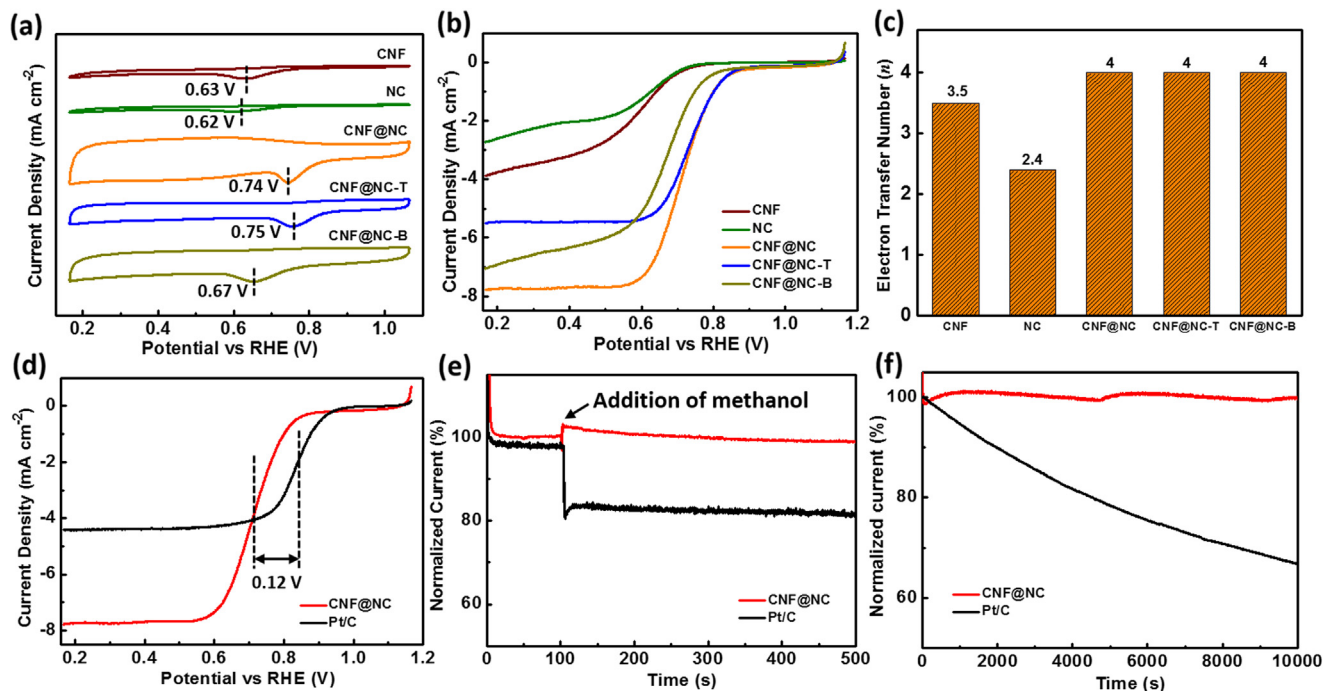
Fig. 5. (a) CV curves of different sample-modified electrodes in O_2-saturated 0.1 M KOH solution with a sweep rate of 5 mV s^{-1}. (b) LSV curves of different sample-modified electrodes at the rotation rate of 1600 rpm in O_2-saturated 0.1 M KOH solution. (c) The calculated electron transfer numbers of different samples. (d) The comparison of the $E_{1/2}$ potentials for the CNF@NC and commercial Pt/C electrode. (e) Chronoamperometric responses of CNF@NC and Pt/C at 0.589 V *vs.* RHE O_2-saturated 0.1 M KOH solution. The arrow indicates the addition of methanol. (f) Chronoamperometric responses of CNF@NC and Pt/C electrode at 0.589 V *vs.* RHE in O_2-saturated 0.1 M KOH solution.

thus prepared are also superior to many previously reported metal-free ORR catalysts in alkaline media.

The methanol tolerance is another criterion to evaluate the performance of the ORR catalysts in methanol fuel cells. As shown in Fig. 5e, the cathodic current of the CNF@NC catalyst almost has no change after the introduction of methanol, which manifests the strong tolerance of CNF@NC towards methanol for potential

applications in direct methanol alkaline fuel cells. Nevertheless, there is a sharp drop for the cathodic current on the Pt/C catalyst due to the distinct methanol oxidation reaction. The long-term stability of the ORR catalyst is assessed by conducting the chronoamperometric measurement of the catalyst-modified electrodes at 0.589 V (*vs.* RHE) in O_2 saturated 0.1 M KOH at a rotation speed of 1600 rpm. As shown in Fig. 5f, the CNF@NC composite still keeps
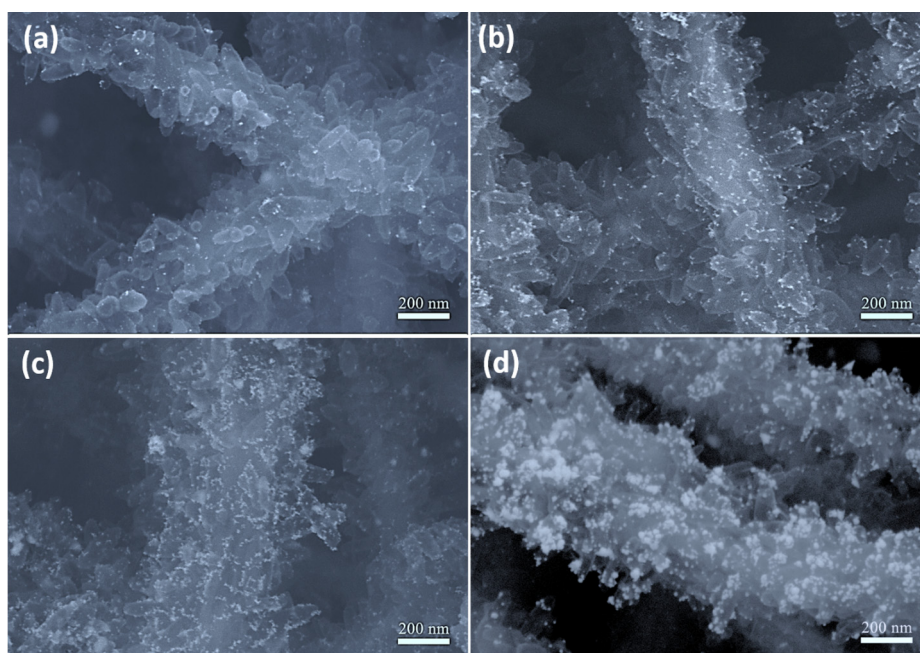

Fig. 6. SEM images of CNF@NC@Pt composites with different loading amounts of Pt nanoparticles. (a) CNF@NC@Pt-5, (b) CNF@NC@Pt-10, (c) CNF@NC@Pt-20, (d) CNF@NC@Pt-30.
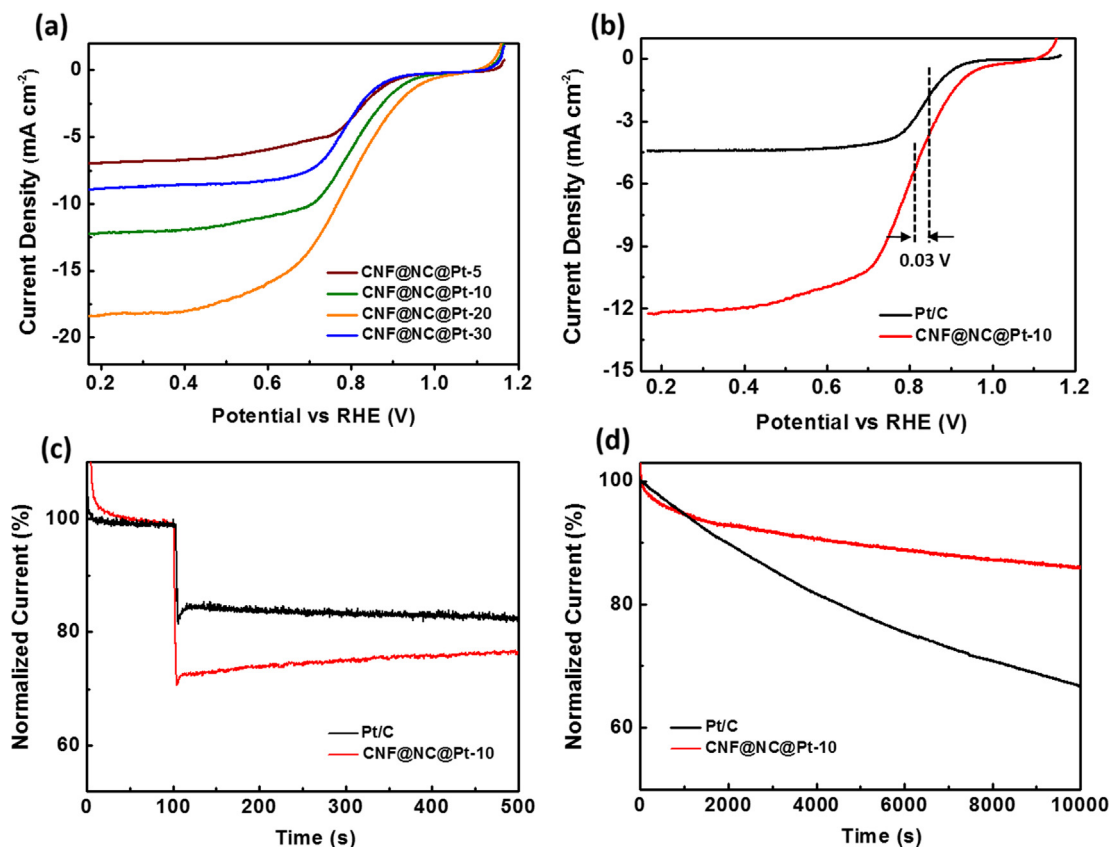
Fig. 7. (a) LSV curves of different CNF@NC@Pt electrodes at the rotation rate of 1600 rpm in O_2-saturated 0.1 M KOH solution. (b) The comparison of the $E_{1/2}$ potentials for the CNF@NC@Pt-10 and commercial Pt/C electrode. (c) Chronoamperometric responses of CNF@NC@Pt-10 and Pt/C at 0.589 V vs. RHE O_2-saturated 0.1 M KOH solution. The arrow indicates the addition of methanol. (d) Chronoamperometric response of CNF@NC@Pt-10 and Pt/C electrode at 0.589 V vs. RHE in O_2-saturated 0.1 M KOH solution.

a high current retention of nearly 100% while the relative current of the commercial Pt/C drops sharply to 67% of its original value after 10 000 s. The good long-term stability of the CNF@NC composite should be ascribed to the highly conductive CNF backbone, which can effectively suppress the structural collapse and active site decrease of the grape-like hollow NC particles.

Ascribed to the excellent catalytic activity and stability of the hierarchical CNF@NC framework, it is further used as a highly conductive template for the decoration of Pt nanoparticles to prepare CNF@NC@Pt composites. As presented in Fig. 6a–c, the bright spots corresponding to Pt nanoparticles are uniformly dispersed on the surface of the CNF@NC frameworks with increasing densities when the concentration of the Pt precursor increases. However, large Pt aggregates are observed when the concentration of the Pt precursor further increases (Fig. 6d), which may lead to the decreased active sites towards oxygen reduction reactions. As expected, the LSV curves of the CNF@NC@Pt composites show gradually positively-shifted onset potentials and increased limited current densities with increasing loading amount of Pt nanoparticles (Fig. 7a). In contrast, there is a sharp decrease in the limited current density of the CNF@NC@Pt-30 composite with a negatively-shifted onset potential, which could be ascribed to the severe aggregation and decreased active sites of Pt nanoparticles. Under a proper loading amount of Pt nanoparticles, the CNF@NC@Pt-10 composite even displays a more positive $E_{1/2}$ value (0.79 V) with only ∼0.03 V deviation compared to the commercial Pt/C catalyst (Fig. 7b). Furthermore, the limited current density (12.0 mA cm^{-2}) of the CNF@NC@Pt-10 composite is almost two times higher than that (4.4 mA cm^{-2}) of the Pt/C catalyst. Besides, the CNF@NC@Pt-10 catalyst also exhibits relatively good methanol tolerance and

long-term stability in alkaline media (Fig. 7c–d), being promising as an excellent low-Pt usage ORR electrocatalyst.

4. Conclusions

In summary, we have developed a simple strategy to prepare a highly integrated carbon nanofiber@nitrogen-doped hollow carbon particle composite by mimicking the bio-inspired hierarchical "grape cluster" superstructure. Ascribed to the robust three-dimensionally connected conductive network, both electron and mass transfer are largely facilitated during the oxygen reduction reactions. Consequently, the as-obtained CNF@NC catalyst presents superior catalytic activity, strong methanol tolerance and good long-term stability towards ORR in alkaline media. Therefore, we believe that the bio-inspired idea and convenient synthesis method can be widely extended for the development of other metal-free carbonaceous materials in efficient electrochemical reactions.

Appendix A. Supplementary material

Supplementary data associated with this article can be found, in the online version, at https://doi.org/10.1016/j.apsusc.2018.02.279.

References

[1] M.H. Shao, Q.W. Chang, J.P. Dodelet, R. Chenitz, Recent advances in electrocatalysts for oxygen reduction reaction, Chem. Rev. 116 (2016) 3594–3657.

[2] H.C. Tao, Y.N. Gao, N. Talreja, F. Guo, J. Texter, C. Yan, Z.Y. Sun, Two-dimensional nanosheets for electrocatalysis in energy generation and conversion, J. Mater. Chem. A 5 (2017) 7257–7284.

[3] W. Wang, F. Lv, B. Lei, S. Wan, M.C. Luo, S.J. Guo, Tuning nanowires and nanotubes for efficient fuel-cell electrocatalysis, Adv. Mater. 28 (2016) 10117–10141.

[4] S. Sui, X.Y. Wang, X.T. Zhou, Y.H. Su, S. Riffat, C.J. Liu, A comprehensive review of Pt electrocatalysts for the oxygen reduction reaction: nanostructure, activity, mechanism and carbon support in PEM fuel cells, J. Mater. Chem. A 5 (2017) 1808–1825.

[5] J. Calderón Gómez, R. Moliner, M. Lázaro, Palladium-based catalysts as electrodes for direct methanol fuel cells: a last ten years review, Catalysts 6 (2016) 130.

[6] J. Masa, W. Xia, M. Muhler, W. Schuhmann, On the role of metals in nitrogen-doped carbon electrocatalysts for oxygen reduction, Angew. Chem. Int. Ed. 54 (2015) 10102–10120.

[7] C.G. Hu, L.M. Dai, Carbon-based metal-free catalysts for electrocatalysis beyond the ORR, Angew. Chem. Int. Ed. 55 (2016) 11736–11758.

[8] Y.E. Miao, F. Li, H.Y. Lu, J.J. Yan, Y.P. Huang, T.X. Liu, Nanocubic-Co$_3$O$_4$ coupled with nitrogen-doped carbon nanofiber network: a synergistic binder-free catalyst toward oxygen reduction reactions, Compos. Commun. 1 (2016) 15–19.

[9] W. Wei, H.W. Liang, K. Parvez, X.D. Zhuang, X.L. Feng, K. Müllen, Nitrogen-doped carbon nanosheets with size-defined mesopores as highly efficient metal-free catalyst for the oxygen reduction reaction, Angew. Chem. 126 (2014) 1596–1600.

[10] D.S. Yu, E. Nagelli, F. Du, L.M. Dai, Metal-free carbon nanomaterials become more active than metal catalysts and last longer, J. Phys. Chem. Lett. 1 (2010) 2165–2173.

[11] B.W. Wang, L.L. Si, J.Y. Geng, Y.H. Su, Y. Li, X.L. Yan, L.G. Chen, Controllable magnetic 3D nitrogen-doped graphene gel: synthesis, characterization, and catalytic performance, Appl. Catal. B – Environ. 204 (2017) 316–323.

[12] Y.J. Gao, G. Hu, J. Zhong, Z.J. Shi, Y.S. Zhu, D.S. Su, J.G. Wang, X.H. Bao, D. Ma, Nitrogen-doped sp2-hybridized carbon as a superior catalyst for selective oxidation, Angew. Chem. Int. Ed. 52 (2013) 2109–2113.

[13] C.T. Zhao, C. Yu, S.H. Liu, J. Yang, X.M. Fan, H.W. Huang, J.S. Qiu, 3D porous N-doped graphene frameworks made of interconnected nanocages for ultrahigh-rate and long-life Li-O$_2$ batteries, Adv. Funct. Mater. 25 (2015) 6913–6920.

[14] S. Kumar, S. Gonen, A. Friedman, L. Elbaz, G.D. Nessim, Doping and reduction of graphene oxide using chitosan-derived volatile N-heterocyclic compounds for metal-free oxygen reduction reaction, Carbon 120 (2017) 419–426.

[15] T.N. Ye, L.B. Lv, X.H. Li, M. Xu, J.S. Chen, Strongly veined carbon nanoleaves as a highly efficient metal-free electrocatalyst, Angew. Chem. Int. Ed. 53 (2014) 6905–6909.

[16] Q. Shi, Y.D. Wang, Z.M. Wang, Y.P. Lei, B. Wang, N. Wu, C. Han, S. Xie, Y.Z. Gou, Three-dimensional (3D) interconnected networks fabricated via in-situ growth of N-doped graphene/carbon nanotubes on co-containing carbon nanofibers for enhanced oxygen reduction, Nano Res. 9 (2016) 317–328.

[17] D. Guo, R. Shibuya, C. Akiba, S. Saji, T. Kondo, J. Nakamura, Active sites of nitrogen-doped carbon materials for oxygen reduction reaction clarified using model catalysts, Science 351 (2016) 361.

[18] Z.X. Xu, X.D. Zhuang, C.Q. Yang, J. Cao, Z.Q. Yao, Y.P. Tang, J. Jiang, D.Q. Wu, X.L. Feng, Nitrogen-doped porous carbon superstructures derived from hierarchical assembly of polyimide nanosheets, Adv. Mater. 28 (2016) 1981–1987.

[19] F.L. Lai, Y.P. Huang, L.Z. Zuo, H.H. Gu, Y.E. Miao, T.X. Liu, Electrospun nanofiber-supported carbon aerogel as a versatile platform toward asymmetric supercapacitors, J. Mater. Chem. A 4 (2016) 15861–15869.

[20] X.H. Li, M. Antonietti, Polycondensation of boron- and nitrogen-codoped holey graphene monoliths from molecules: carbocatalysts for selective oxidation, Angew. Chem. 125 (2013) 4670–4674.

[21] Y. Zhao, C.G. Hu, Y. Hu, H.H. Cheng, G.Q. Shi, L.T. Qu, A. Versatile, Ultralight, nitrogen-doped graphene framework, Angew. Chem. Int. Ed. 51 (2012) 11371–11375.

[22] K. Sakaushi, M. Antonietti, Carbon- and nitrogen-based organic frameworks, Acc. Chem. Res. 48 (2015) 1591–1600.

[23] X.H. Li, M. Antonietti, Metal nanoparticles at mesoporous N-doped carbons and carbon nitrides: functional Mott-Schottky heterojunctions for catalysis, Chem. Soc. Rev. 42 (2013) 6593–6604.

[24] D. Zhao, S.W. Liu, X.W. Peng, H. Hu, H.Q. Hou, The preparation of electrospun self-supporting silicon-containing hole carbon nanofibers and their application in high-performance lithium-ion battery anode materials, J. Jiangxi Normal Univ. 3 (2014) 290–294.

[25] H.W. Liang, W. Wei, Z.S. Wu, X. Feng, K. Müllen, Mesoporous metal–nitrogen-doped carbon electrocatalysts for highly efficient oxygen reduction reaction, J. Am. Chem. Soc. 135 (2013) 16002–16005.

[26] J.M. Jeong, K.G. Lee, S.J. Chang, J.W. Kim, Y.K. Han, S.J. Lee, B.G. Choi, Ultrathin sandwich-like MoS$_2$@N-doped carbon nanosheets for anodes of lithium ion batteries, Nanoscale 7 (2015) 324–329.

[27] J.J. Yan, H.Y. Lu, Y.P. Huang, J. Fu, S.Y. Mo, C. Wei, Y.E. Miao, T.X. Liu, Polydopamine-derived porous carbon fiber/cobalt composites for efficient oxygen reduction reactions, J. Mater. Chem. A 3 (2015) 23299–23306.

[28] J.J. Yan, Y.F. Zhang, Y.P. Huang, Y.E. Miao, T.X. Liu, MoSe$_2$ nanosheets grown on polydopamine-derived porous fibers: a high-performance catalyst for hydrogen evolution reaction, Adv. Mater. Interf. 4 (2017) 1600825.

[29] X. Ge, Y. Ma, X.Y. Song, G.Z. Wang, H.M. Zhang, Y.X. Zhang, H.J. Zhao, β-FeOOH nanorods/carbon foam-based hierarchically porous monolith for highly effective arsenic removal, ACS Appl. Mater. Interf. 9 (2017) 13480–13490.

[30] G. Park, Y.I. Kim, Y.H. Kim, M. Park, K.Y. Jang, H. Song, K.M. Nam, Preparation and phase transition of FeOOH nanorods: strain effects on catalytic water oxidation, Nanoscale 9 (2017) 4751–4758.

[31] M. Zhang, Y.H. Liu, Z.R. Shang, H.C. Hu, Z.H. Zhang, Supported molybdenum on graphene oxide/Fe$_3$O$_4$: an efficient, magnetically separable catalyst for one-pot construction of spiro-oxindole dihydropyridines in deep eutectic solvent under microwave irradiation, Catal. Commun. 88 (2017) 39–44.

[32] X.H. Xia, Y.D. Wang, D.H. Wang, Y.Q. Zhang, Z.X. Fan, J.P. Tu, H. Zhang, H.J. Fan, Atomic-layer-deposited iron oxide on arrays of metal/carbon spheres and their application for electrocatalysis, Nano Energy 20 (2016) 244–253.

[33] D.S. Geng, Y. Chen, Y.G. Chen, Y.L. Li, R.Y. Li, X.L. Sun, S.Y. Ye, S. Knights, High oxygen-reduction activity and durability of nitrogen-doped graphene, Energy Environ. Sci. 4 (2011) 760–764.

[34] Y.H. Su, Y.H. Zhu, H.L. Jiang, J.H. Shen, X.L. Yang, W.J. Zou, J.D. Chen, C.Z. Li, Cobalt nanoparticles embedded in N-doped carbon as an efficient bifunctional electrocatalyst for oxygen reduction and evolution reactions, Nanoscale 6 (2014) 15080–15089.

[35] D.S. Yu, Q. Zhang, L.M. Dai, Highly efficient metal-free growth of nitrogen-doped single-walled carbon nanotubes on plasma-etched substrates for oxygen reduction, J. Am. Chem. Soc. 132 (2010) 15127–15129.

[36] Y.P. Zhu, C. Guo, Y. Zheng, S.Z. Qiao, Surface and interface engineering of noble-metal-free electrocatalysts for efficient energy conversion processes, Acc. Chem. Res. 50 (2017) 915–923.